IN 34

179676

39 P

HYPERSONIC, NONEQUILIBRIUM FLOW OVER A CYLINDRICALLY BLUNTED 6° WEDGE

Peter A. Gnoffo

August 1993

Hypersonic, Nonequilibrium Flow over a Cylindrically Blunted 6° Wedge

Peter A. Gnoffo
NASA Langley Research Center
Hampton, VA 23681-0001

SUMMARY

The numerical simulation of hypersonic flow in chemical nonequilibrium over a cylindrically blunted 6° wedge is described. The simulation was executed on a Cray C-90 wih Program LAURA-92-v1. Code setup procedures and sample results, including grid refinement studies and variation of species number, are discussed. This simulation relates to a study of wing leading edge heating on transatmospheric vehicles.

VERSION

The $\underline{L}$angley $\underline{A}$erothermodynamic $\underline{U}$pwind $\underline{R}$elaxation $\underline{A}$lgorithm (LAURA-92-v1) is described in References [1] and [2].

CONFIGURATION

The configuration is a two-dimensional, cylindrically blunted wedge. The wedge half-angle θ_c equals 6 degrees. The cylinder nose radius R_N equals 0.125 ft. The wedge length L equals 37.5 ft.

SURFACE GRID

The surface grid is defined with (80x1) cells. The grid was generated automatically by choosing option 2 for geometry initialization in Program Start-92-v1. "Subroutine wingbdy" was used in place of "subroutine elpcone" in line 333 of file "aaa.f" of Program LAURA for geometry initialization. (This substitution was convenient because "subroutine elpcone" currently ignores the geometry options specified in the initialization from Program Start-92-v1.)

Three surface grids were generated. The baseline settings in "wingbdy" call for 15 equally spaced mesh points on the nose and cell growth factor "zfac" equal to 1.2 along the wedge. Baseline settings were used to define "surface.01" The cell growth factor "zfac" was changed to 1.1 in line 20 of file "wingbdy" in order to improve resolution of the expansion off the nose onto the wedge. This setting was used to define "surface.02". The number of mesh points on the nose was increased to 30 in order to check grid convergence in the stagnation region by changing "i1" in line 22 of file "wingbdy". The new settings for both "zfac" and "i1" were used to define "surface.03". The full configuration length could not be spanned by 80 cells using the settings for "surface.03". Surface grid distribution can be deduced from the volume grids shown in Figures 1 - 7.

VOLUME GRID

The volume grid is automatically generated and periodically adjusted within Program LAURA-92-v1. Converged solutions were obtained with 64 cells and 128 cells across the shock layer. Two baseline settings for volume grid adaption were changed for these simulations. The baseline setting in "subroutine algnshk" produces a cell Reynolds number equal to 0.1 at the wall, which recent tests [3] have shown is much smaller than necessary. The cell Reynolds number was set to 1.0 by changing line 83 of file "algnshk.f" from "hmin1=.1*amua(i,j,1)..." to "hmin1=amua(i,j,1)...". Moderate clustering of grid across the shock front was also implemented by changing line 107 of file "algnshk.f" from "ep0=0." to "ep0=25./8.". Global and detail views of the volume grids are presented in Figures 1 - 7.

FREESTREAM CONDITIONS

Only one set of freestream conditions were tested as shown in Table 1.

Table 1 - Freestream Conditions

condition	V_∞ m/s	ρ_∞, kg/m^3	T_∞, K	h, km	M_∞
01	8233.7	7.0626 10^{-4}	270.	53.3	25.

GAS MODEL

The test gas is air in thermal equilibrium and chemical nonequilibrium. The laminar, thin-layer Navier-Stokes option was selected for all cases. Both a 7 species and 11 species air model were tested. The seven species analyses include N, O, N_2, O_2, NO, NO^+, and e^-. The eleven species analyses include the species listed above plus N^+, O^+, N_2^+, O_2^+. The baseline gas kinetic model ("kmodel" set to 3 in line 23 of file "air.f") is substantially derived from the work of Park as detailed in Table 1 of Reference [4].

2

BOUNDARY CONDITIONS

Most of the boundary conditions were set automatically when the self start geometry option 2 was chosen within the initialization of Program Start-92-v1. In addition, a constant wall temperature equal to 1255.6 K and a fully catalytic wall option are specified during the program initialization.

NUMERICAL PARAMETERS

Standard, baseline settings for numerical parameters and options in LAURA are: eigenvalue limiter $\epsilon_0 = 0.30$ with aspect ratio scaling across the boundary layer, and upwind limiter function as defined in Ref. [5]. No changes to these parameters were made for any of the test cases.

TEST MATRIX

The test cases are defined in Table 2.

Table 2 - Test Matrix

case number	freestream conditions	surface configuration	volume grid	gas model	boundary conditions
01	01	surface.01	64 cells	11 species	unchanged
02	01	surface.02	64 cells	11 species	unchanged
03	01	surface.02	64 cells	7 species	unchanged
04	01	surface.02	128 cells	7 species	unchanged
05	01	surface.03	64 cells	7 species	unchanged

SAMPLE RUN LOG

A record of the data file state from run to run for case 05 is included in Table 3.

Table 3 - Data File Log

run	newjob	nord	ifrozen	itervmax	niterp	iterg	moveg	epsa0	errd	rfit	rfvt
01	2	0	1	1	1	100	20	0.3	0.01	2.00	1.00
02 - 03	0	1	1	10	10	1000	10	0.3	0.01	1.51	0.51
04 - 05	0	1	1	10	10	1000	20	0.3	0.10	1.51	0.51
06 - 15	0	1	1	10	10	1000	0	0.3	0.10	1.51	0.51

After the self-start run with "newjob" = 2, the inviscid and viscous relaxation factors were dropped to near minimum values (1.51 and 0.51) based on the excellent stability characteristics observed earlier in cases 01-04. It became clear after run 03 that the error norm for redoubling the grid and the number of iterations available between grid realignments were too restrictive for this case. Consequently, the value of "moveg" was increased to 20 (allowing 200 iterations between realignments) and the error norm criteria for grid doubling "errd" was increased to 0.10. With these settings, the grid doubled from 16 cells to 32 cells after 940 iterations of run 04 and from 32 cells to 64 cells after 380 iterations in run 05. Realignment was automatically switched off after 940 iterations in run 05 when the error norm dropped below "errd" with 64 cells. The realignment flag was then switched off ("moveg" = 0) for runs 06-15 and the multitasking option was switched on by setting "mtask" = 1 in the include file "task1.zzzz", touching file "aaa.f", and recompiling by running "make". (The file "aaa.f" and the common block "btask" were edited to allow for a maximum of 16 processors instead of 8. The value of "ntasks" was changed from 8 to 10 in line 481 of file "aaa.f". The use of 10 processors on the C-90 for this relatively small job (less than 2MW) appeared to give a good mix of concurrent processor usage and job turnaround time in a multiuser environment.)

The error norm dropped nearly uniformly from $7 \ 10^{-3}$ to $2 \ 10^{-8}$ between runs 06 and 15, with each run requiring approximately 30 concurrent CPU seconds. The change in stagnation point heating between runs 08 and 09 was less than 1.2% and between runs 14 and 15 was less than 0.046%. The change in trailing edge heating was less than 0.75% between runs 14 and 15.

Run logs for the earlier cases were not recorded in detail. The only difference believed to be of significance is that the value of "errd" was set to 0.2 on or about the fourth run, based on observing the rate and behavior of the error norm history. The earlier cases included the entire wedge length and may account for the slightly altered convergence characteristics. Also case 04 was started directly from a converged case 03 by changing the value of "kaq' in file "parml.zzzz" from 64 to 128 and recompiling after touching all of the "*.f" files. Mesh points were placed halfway between meshpoints from case.04.

RESULTS

The effect of surface grid distribution on convective heating for the 11 species model is presented in Figure 8. Differences in heating levels are only observed far downstream from the nose, and are less than 8%. There is no significant difference between the convective heating distribution resulting from the 11 species and 7 species air models, as shown in Figure 9. The effect of surface and volume grid distribution on convective heating for the 7 species model is presented in Figure 10. A detail view of the nose region shows a fully grid converged solution with regard to surface heating in Figure 11.

Shock layer profiles taken from cell centers adjacent to the stagnation streamline are presented for cases 03 - 05 in Figures 12 - 17. The cell centers for cases 03 and 04 are offset approximately 3° from the stagnation streamline and cell centers from case 05 are offset approximately 1.5°. The symbols which appear on some figures indicate the grid point locations. Log scales are included in some figures to highlight the boundary layer effects. Results here show almost no effect due to variations in grid distribution. The largest differences occur in temperature across the captured

shock front (Figure 14 where case 04 with 128 cells gives a sharper resolution of the front. A highly magnified pressure profile in Figure 13 shows a slight wiggle deep in the boundary layer for cases 03 and 05 (64 cells) which is not present in case 04 (128 cells). This behavior may be caused by the magnitude of the stretching factors in this vicinity as defined from within "subroutine algnshk".

A pressure contour plot over the forward part of the blunted wedge is presented in Figure 18. The upper symmetry plane is from case 04 and the lower symmetry plane is from case 05. The variation in pressure across the boundary layer as seen earlier in Figure 13 is evident here as well.

Boundary layer profiles in the exit plane from cases 03 and 04, on the same surface grid, are presented in Figures 19 - 32. The profiles for temperature 23, 24 and density 21, 22 show a dependence on grid resolution. There is structure near the peak temperature in the boundary layer from case 04 that is absent in the coarser resolution from case 03. There is a local maximum in the total enthalpy at the boundary layer edge, slightly higher than the freestream value, which appears to be grid converged.

CONCLUSIONS

The heating results presented here are grid converged in the nose region and show a maximum difference of 8% as a function of grid at the trailing edge. The differences between a 7 species model and an 11 species model are inconsequential with regard to the effect on convective heating.

REFERENCES

[1] Gnoffo, Peter A.; Gupta, Roop N.; and Shinn, Judy: "Conservation Equations and Physical Models for Hypersonic Air Flows in Thermal and Chemical Nonequilibrium," NASA TP 2867, February 1989.

[2] Gnoffo, Peter A., "Point-Implicit Relaxation Strategies for Viscous, Hypersonic Flows," in Computational Methods in Hypersonic Aerodynamics, T.K.S. Murthy, ed., Computational Mechanics Publications, Kluwer Academic Publishers, pp 115-151, 1991.

[3] Gnoffo, Peter A.; Hartung, Lin C.; and Greendyke, Robert B.: "Heating Analysis for a Lunar Transfer Vehicle at Near-Equilibrium Flow Conditions," AIAA 93-0270, January 1993.

[4] Park, Chul; Howe, John T.; Jaffe, Richard L.; and Candler, Graham V.: "Chemical-Kinetic Problems of Future NASA Missions ", AIAA 91-0464, January 1991.

[5] Weilmuenster, K. James; and Gnoffo, Peter A.: "Solution Strategies and Heat Transfer Calculations for Three-Dimensional Configurations at Hypersonic Speeds," AIAA 92-2921, July, 1992.
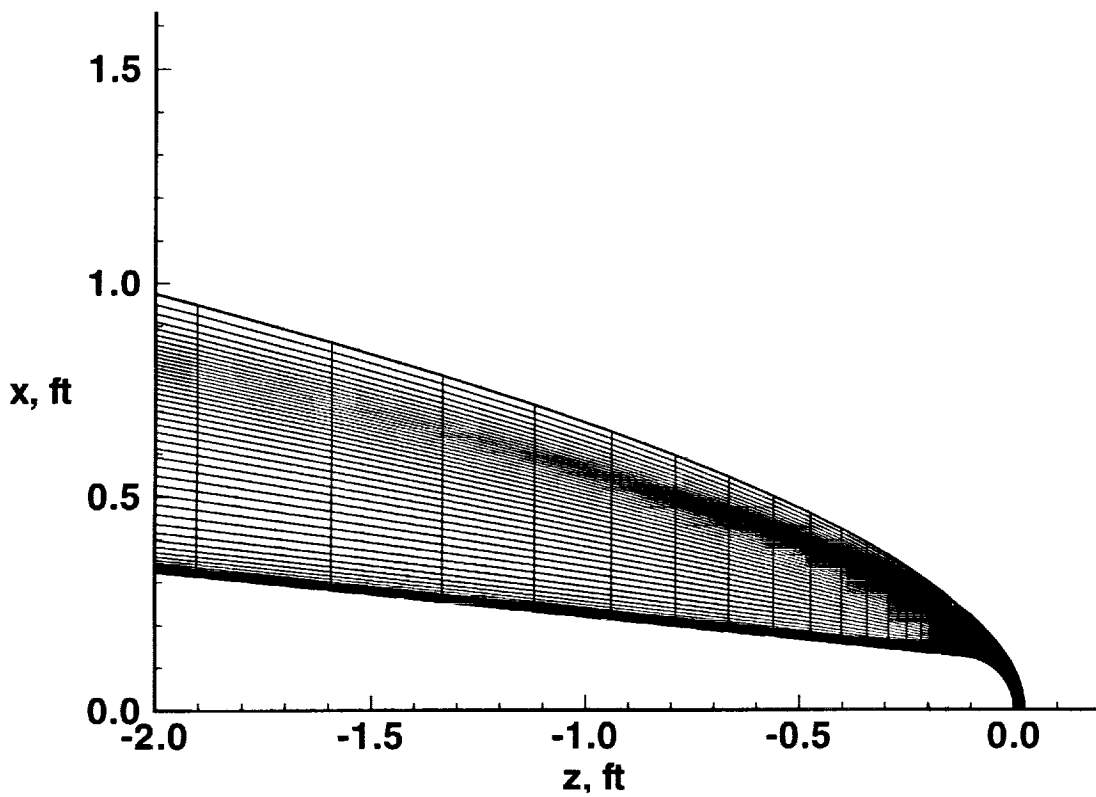
Figure 1: Detail of volume grid for case 01 on surface.01. The cell width Δz grows by a factor of 1.2 after equal spacing with 15 points on the cylindrical nose. There are 64 cells across the shock layer with moderate clustering at the captured shock.
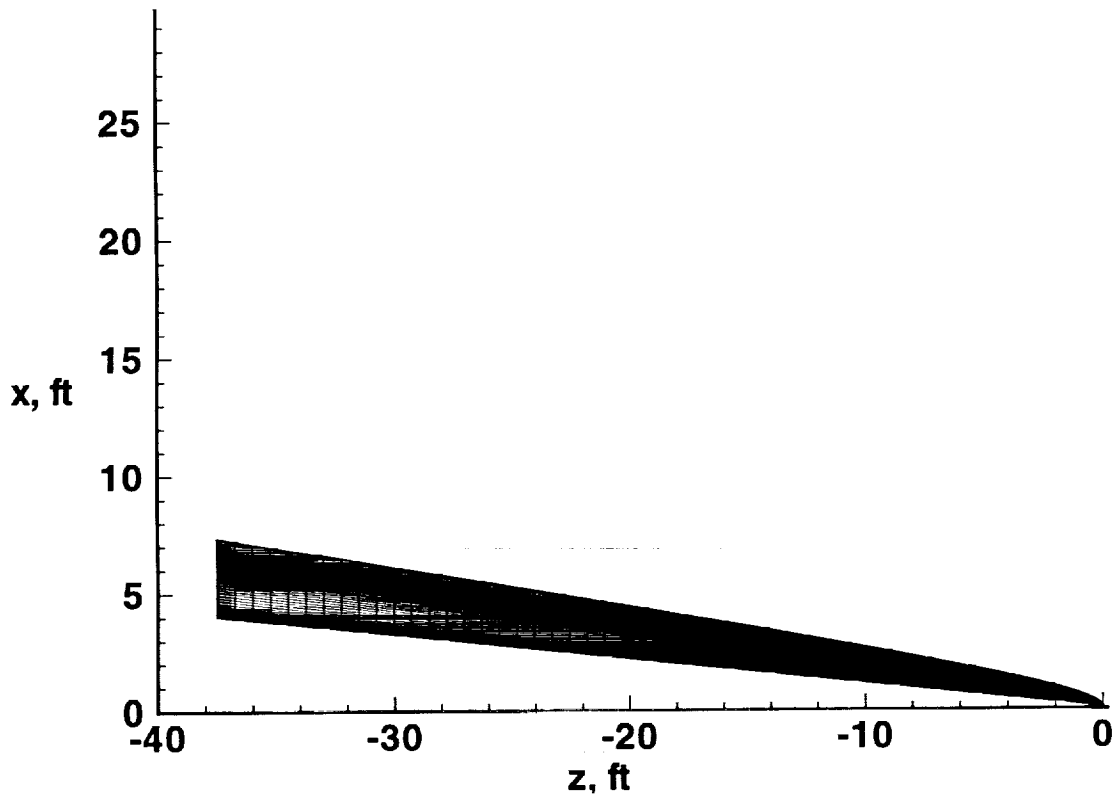
Figure 2: Volume grid for case 01 on surface.01. The cell width Δz grows by a factor of 1.2 after equal spacing with 15 points on the cylindrical nose. There are 64 cells across the shock layer with moderate clustering at the captured shock and 80 cells around the body.
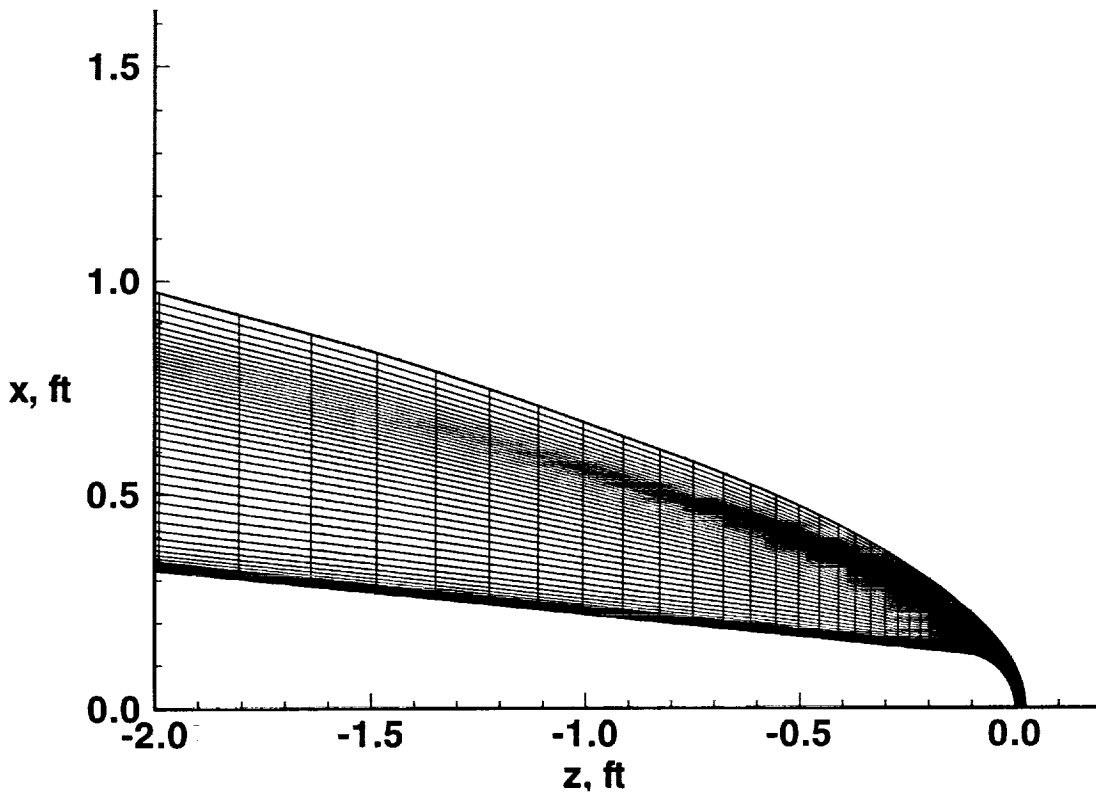
Figure 3: Detail of volume grid for cases 02 and 03 on surface.02. The cell width Δz grows by a factor of 1.1 after equal spacing with 15 points on the cylindrical nose. There are 64 cells across the shock layer with moderate clustering at the captured shock.
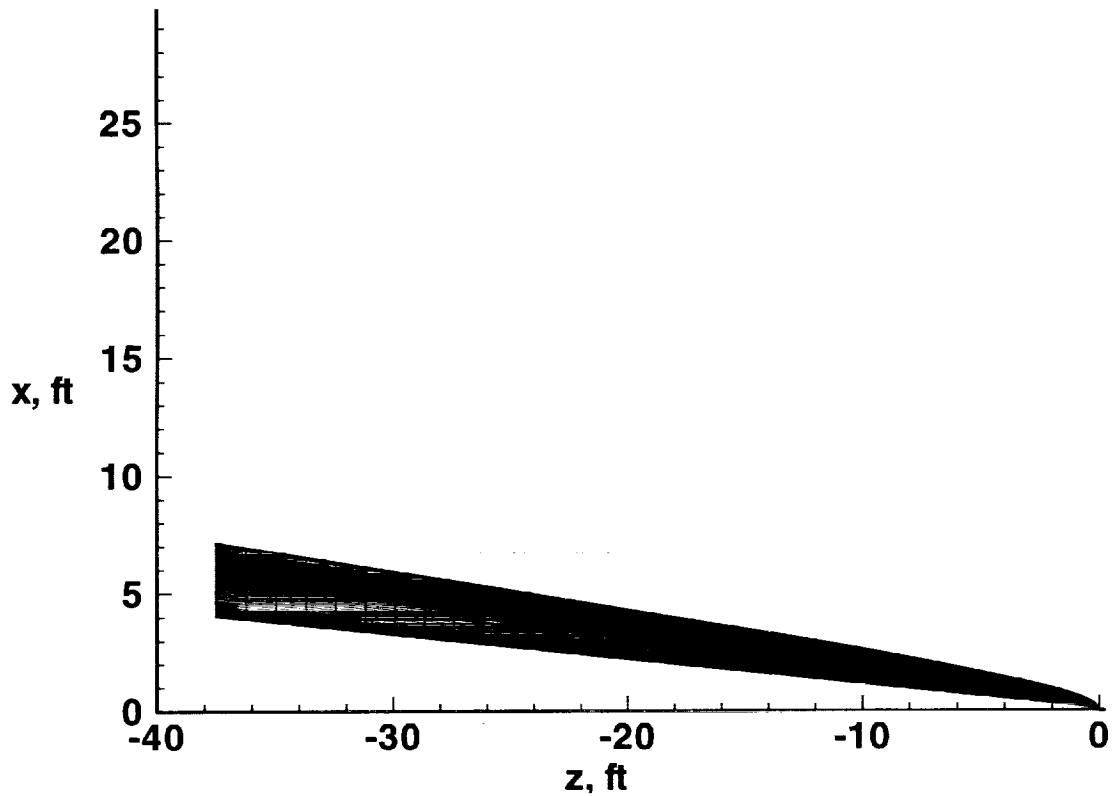
Figure 4: Volume grid for cases 02 and 03 on surface.02. The cell width Δz grows by a factor of 1.1 after equal spacing with 15 points on the cylindrical nose. There are 64 cells across the shock layer with moderate clustering at the captured shock and 80 cells around the body.
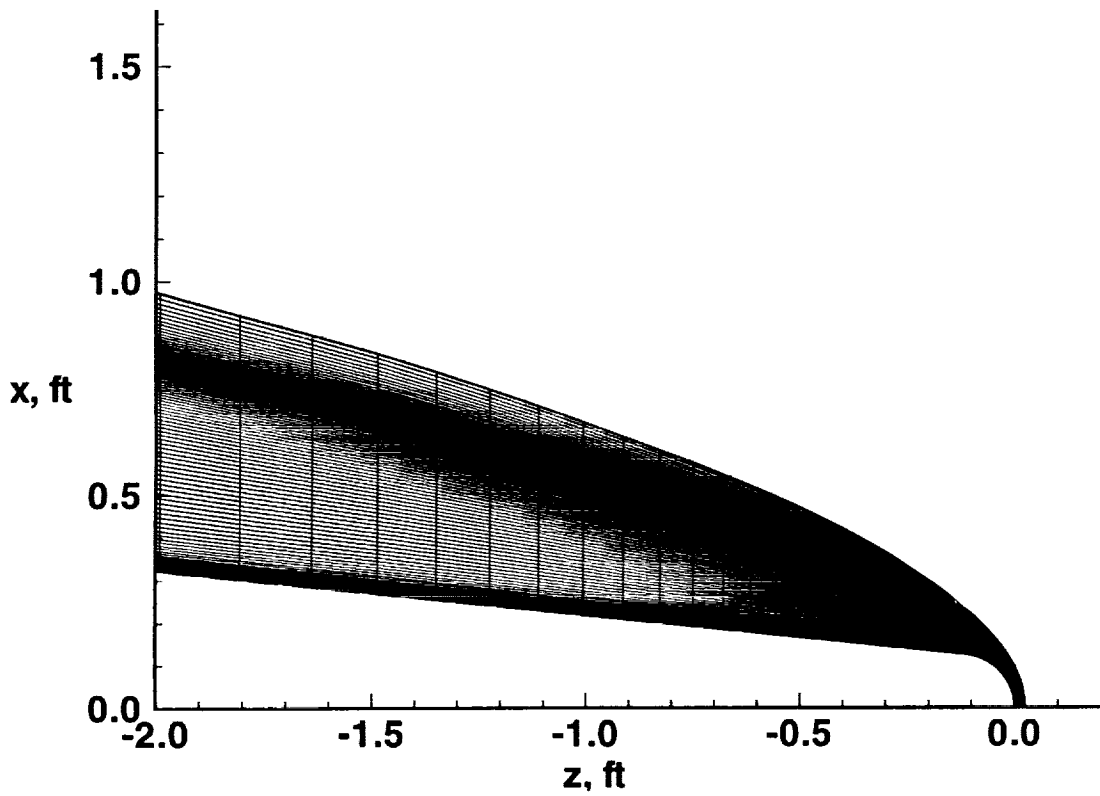
Figure 5: Detail of volume grid for case 04 on surface.02. The cell width Δz grows by a factor of 1.1 after equal spacing with 15 points on the cylindrical nose. There are 128 cells across the shock layer with moderate clustering at the captured shock.
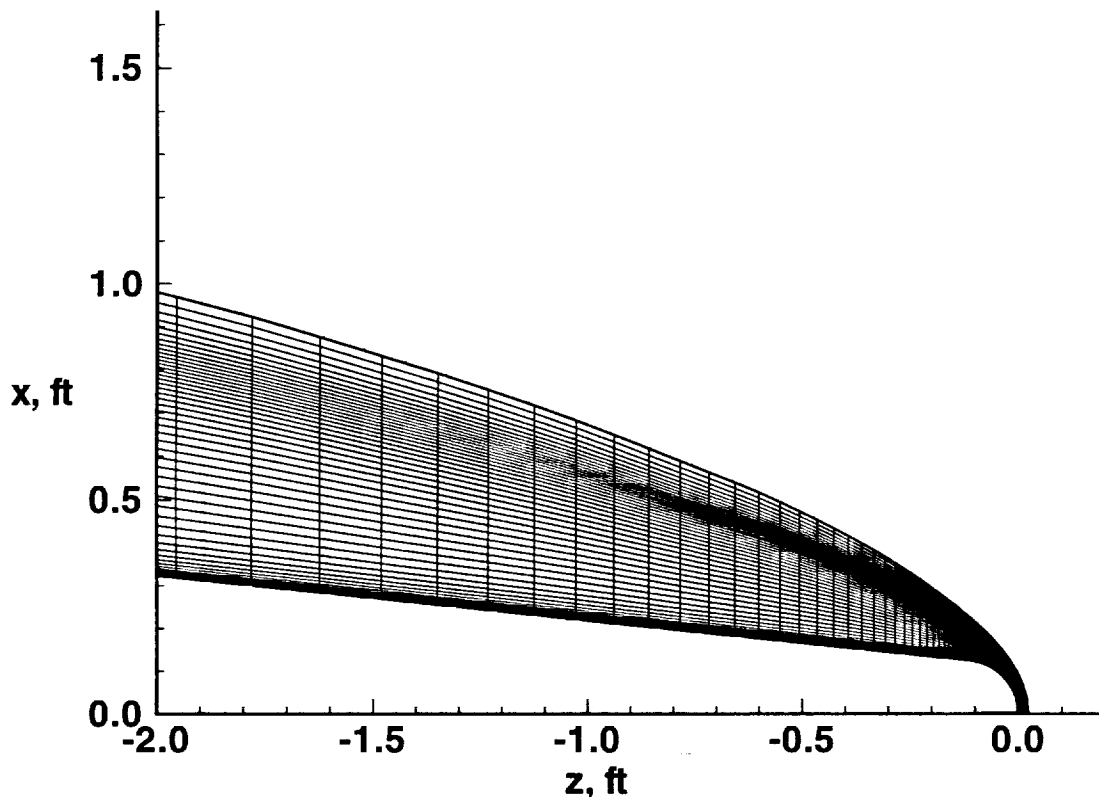
Figure 6: Detail of volume grid for case 05 on surface.03. The cell width Δz grows by a factor of 1.1 after equal spacing with 30 points on the cylindrical nose. There are 64 cells across the shock layer with moderate clustering at the captured shock.
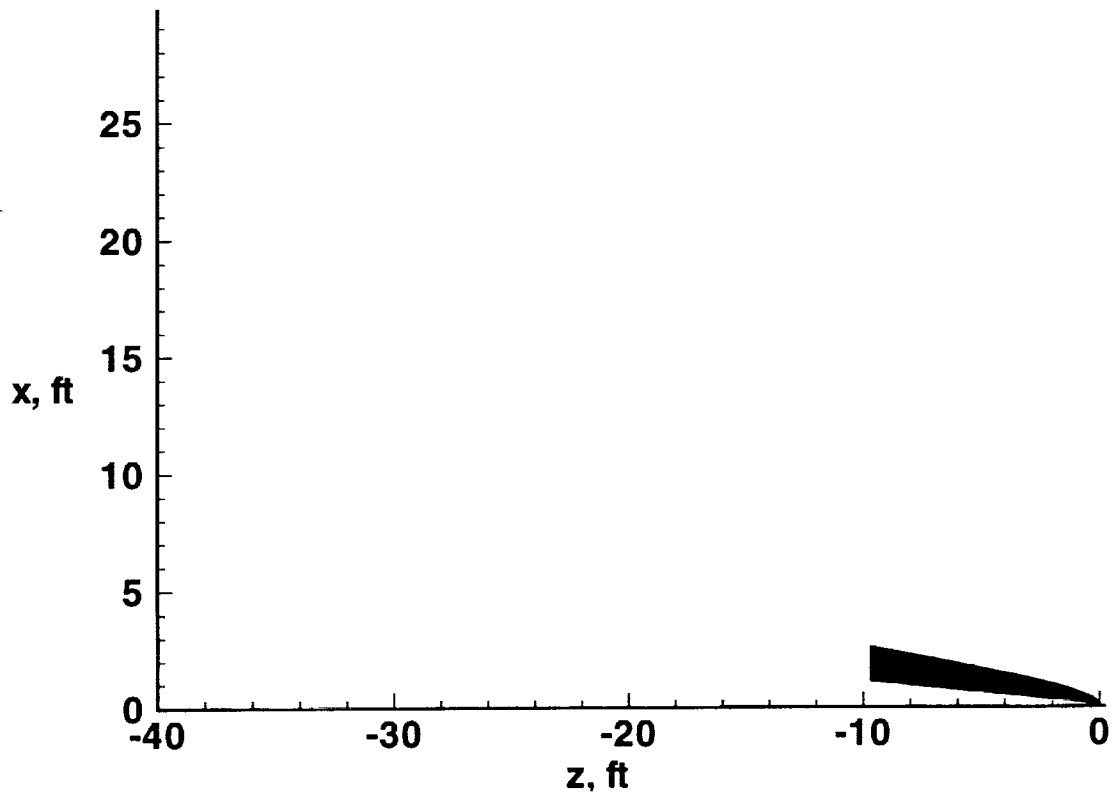
Figure 7: Volume grid for case 05 on surface.03. The cell width Δz grows by a factor of 1.1 after equal spacing with 30 points on the cylindrical nose. There are 64 cells across the shock layer with moderate clustering at the captured shock and 80 cells around the body. The surface grid settings force all resolution on the forward part of the wedge.
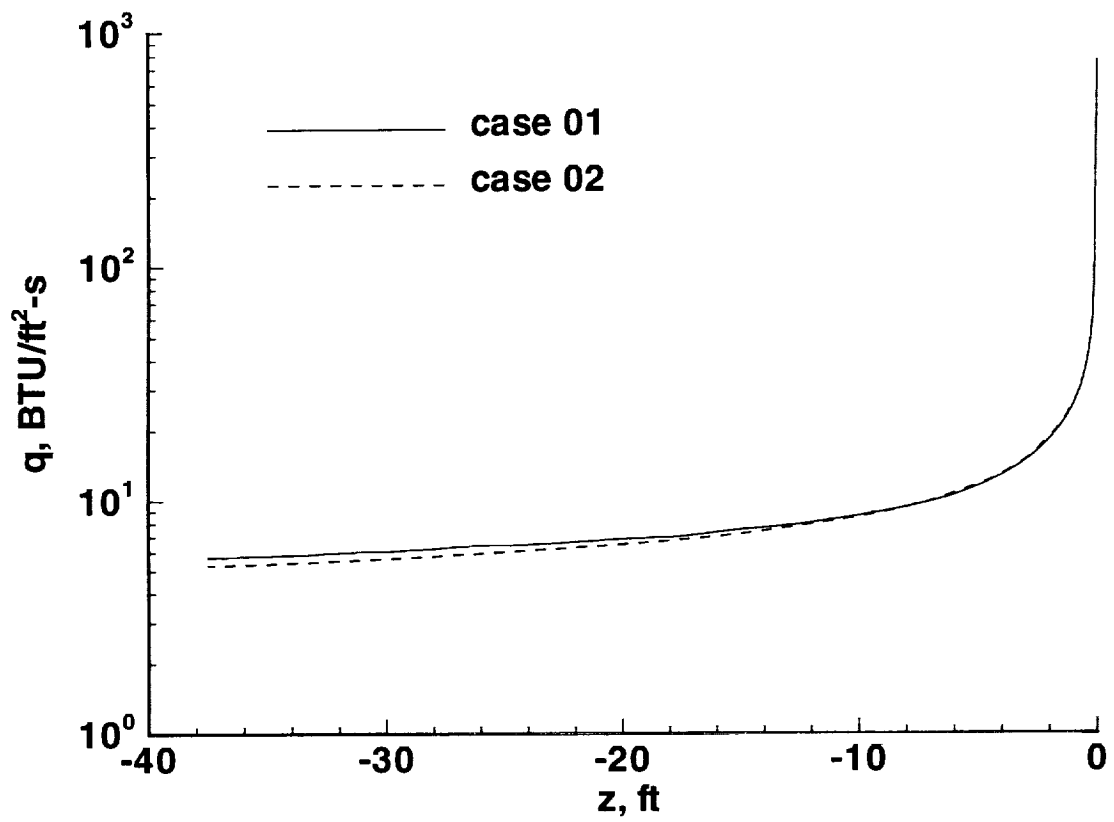
Figure 8: Convective heating distribution for cases 01 and 02 involving 11 species on surface.01 and surface.02, respectively.
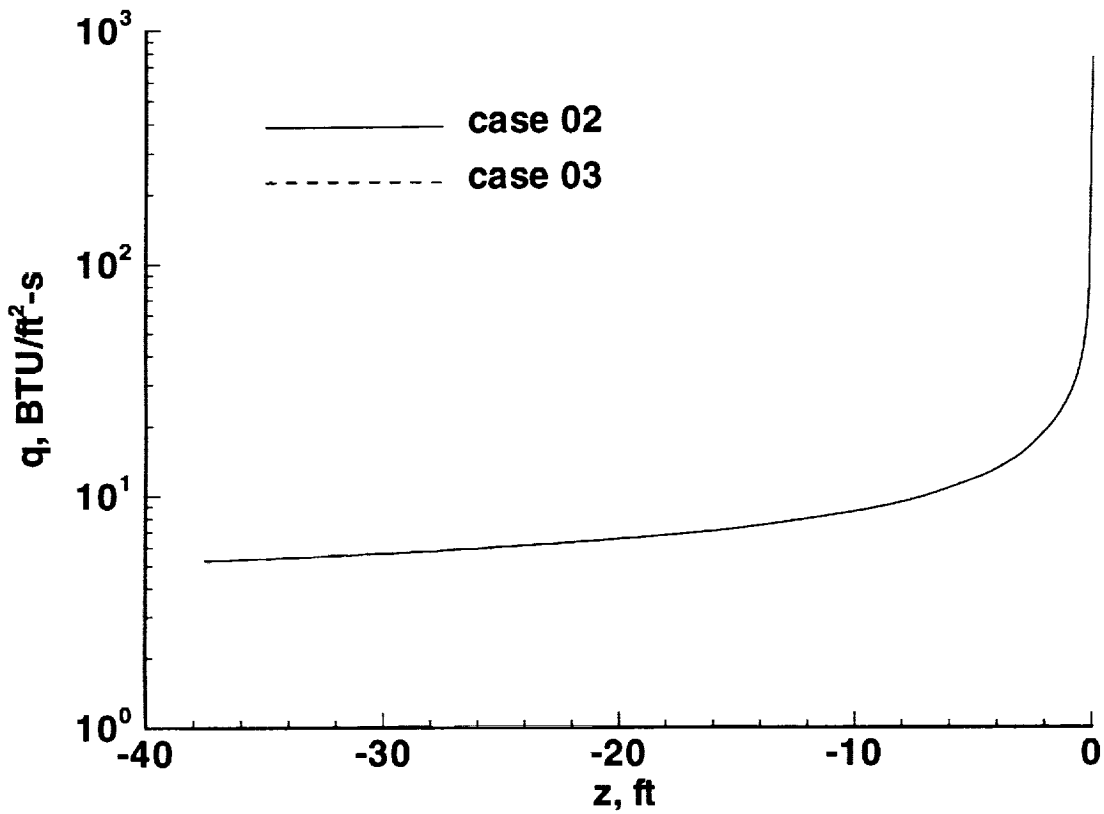
Figure 9: Convective heating distribution for cases 02 and 03 for the 11 species and 7 species air models, respectively, computed on the same volume grid over surface.02.
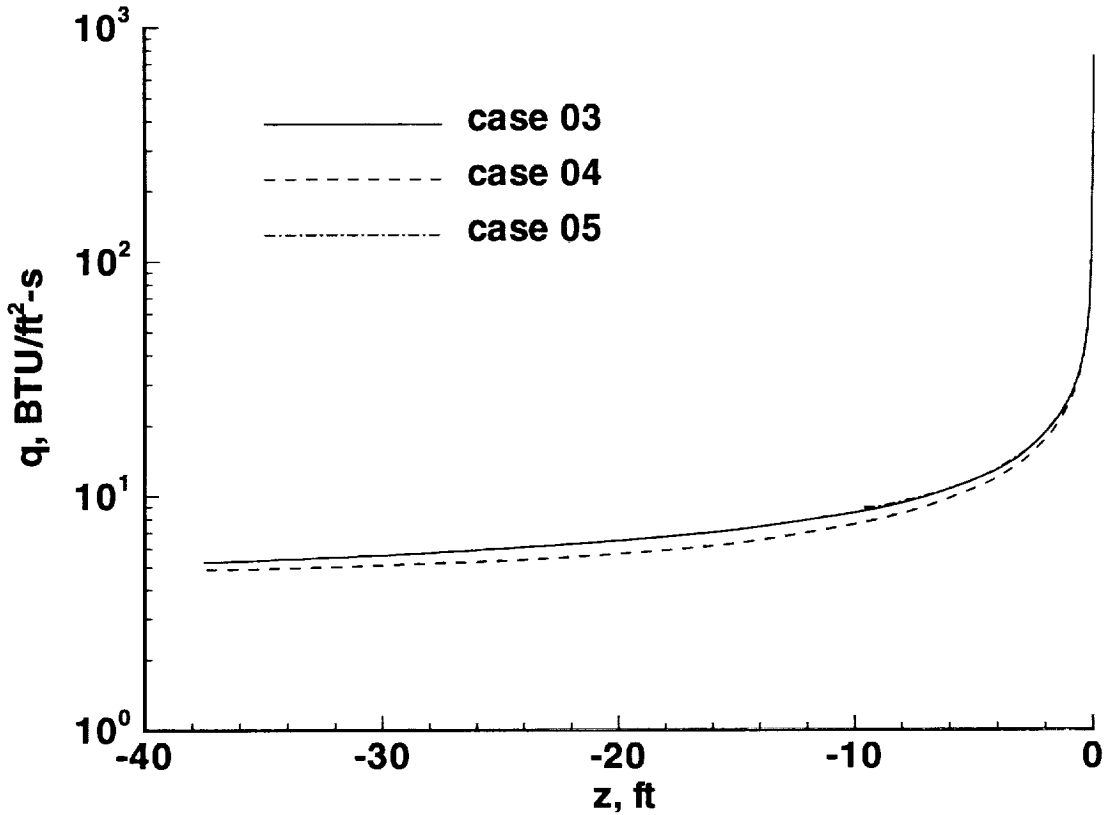
Figure 10: Convective heating distribution for cases 03, 04, and 05 involving a 7 species air model. Cases 03 and 04 are computed on surface.02 with 64 cells and 128 cells , respectively, spanning the shock layer. Case 05 is computed on surface.03, providing a finer resolution of the nose region, with 64 cells spanning the shock layer.
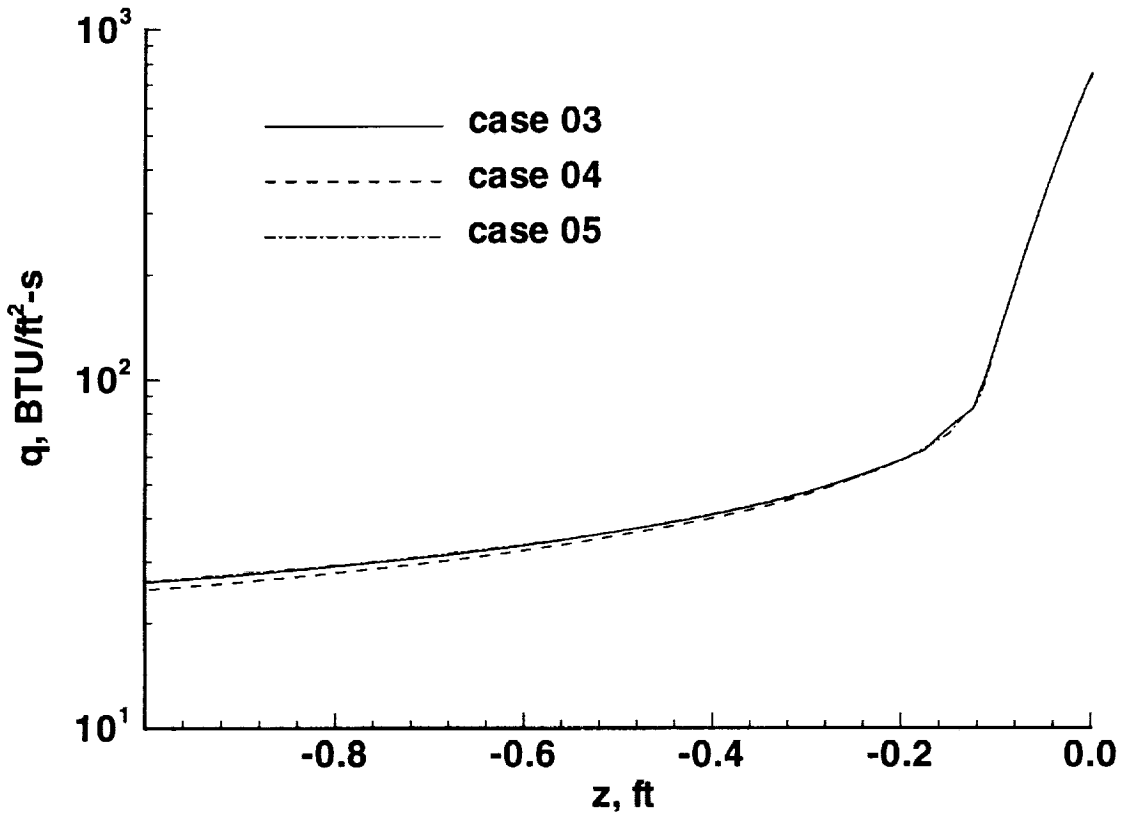
Figure 11: Detail view in nose region of convective heating distribution for cases 03, 04, and 05 involving a 7 species air model. Cases 03 and 04 are computed on surface.02 with 64 cells and 128 cells , respectively, spanning the shock layer. Case 05 is computed on surface.03, providing a finer resolution of the nose region, with 64 cells spanning the shock layer.
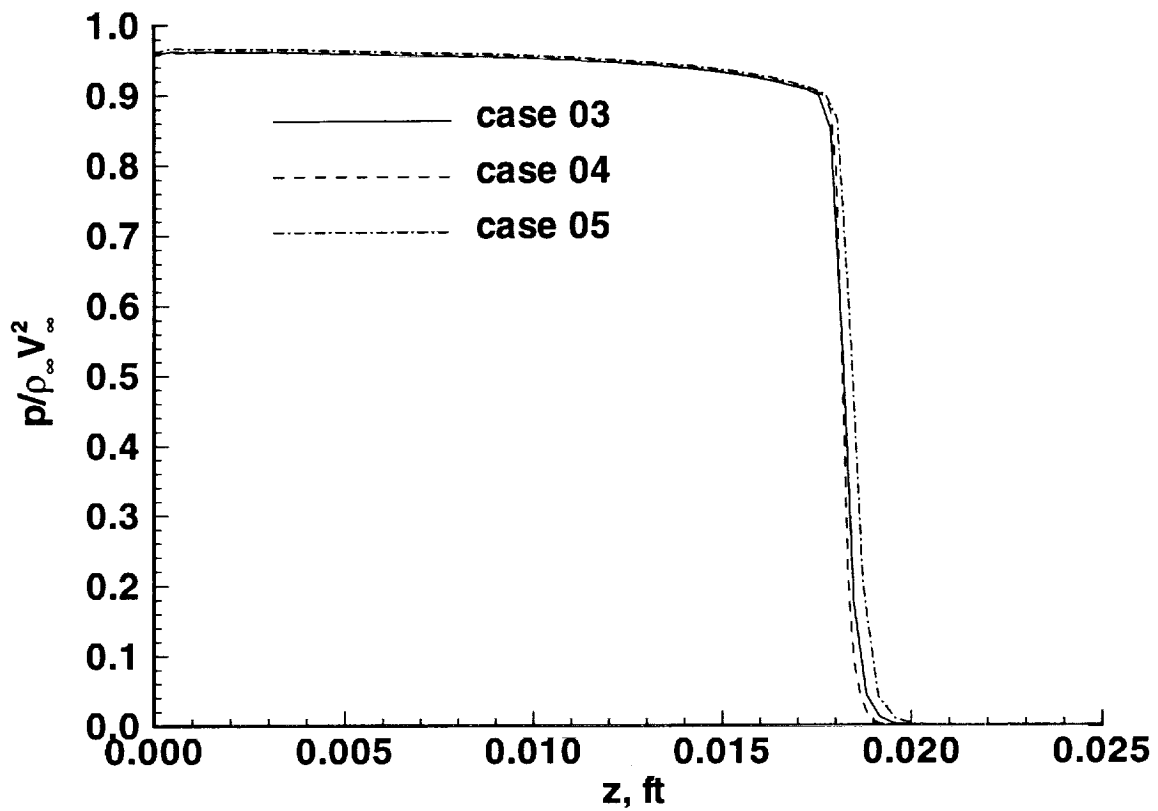
Figure 12: Pressure profile across shock layer adjacent to the stagnation streamline for cases 03, 04 and 05 involving a 7 species air model.
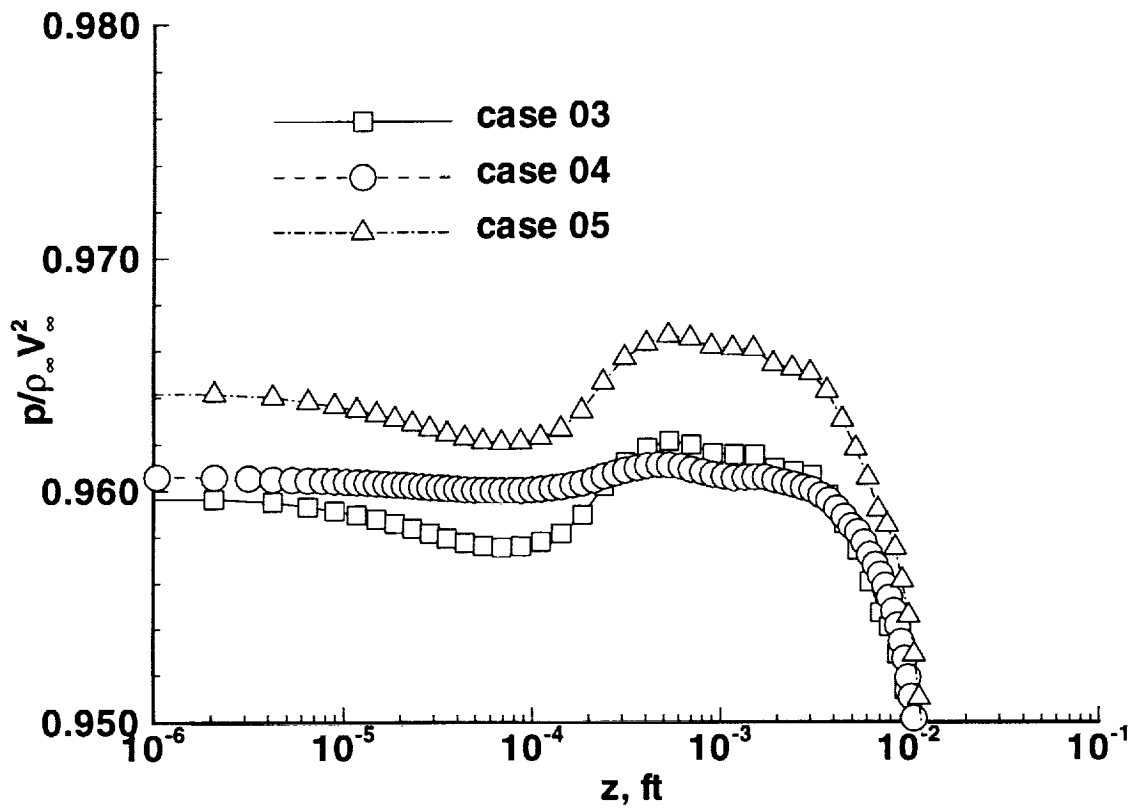
Figure 13: Pressure profile across shock layer adjacent to the stagnation streamline for cases 03, 04 and 05 involving a 7 species air model using a log scale to highlight behavior in the boundary layer. Grid point locations are denoted by symbols.

18
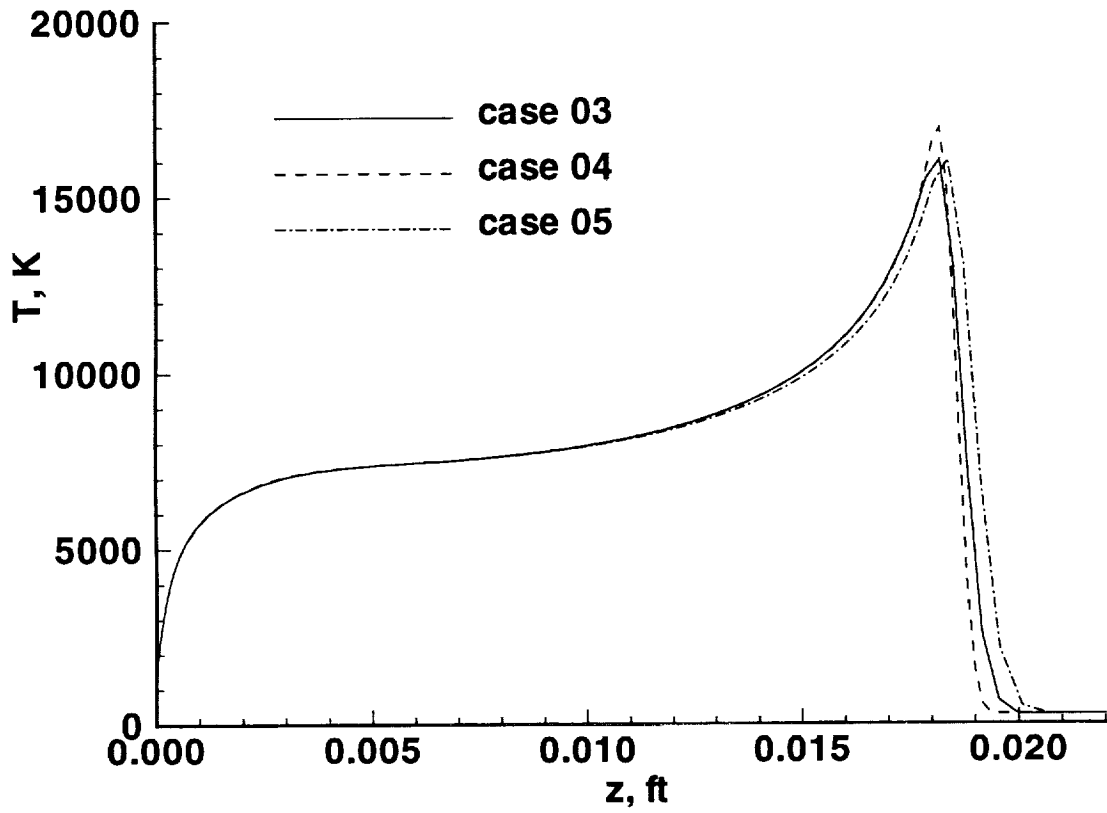
Figure 14: Temperature profile across shock layer adjacent to the stagnation streamline for cases 03, 04 and 05 involving a 7 species air model.
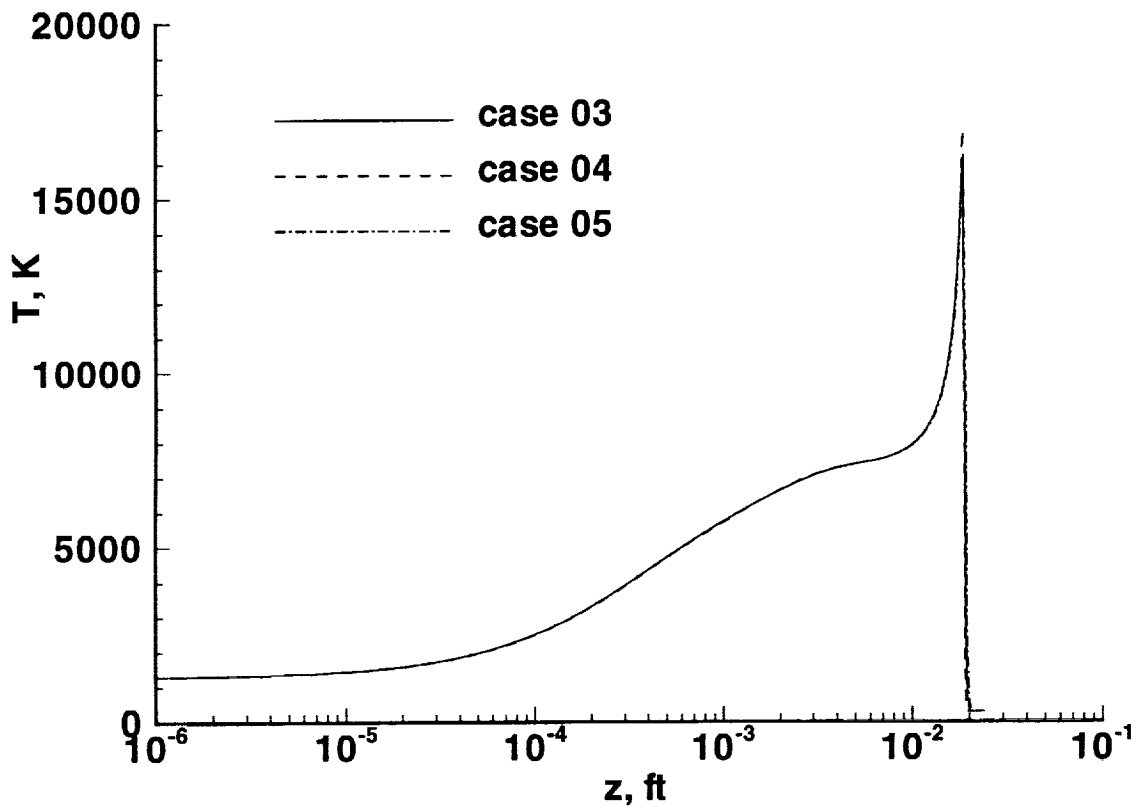
Figure 15: Temperature profile across shock layer adjacent to the stagnation streamline for cases 03, 04 and 05 involving a 7 species air model using a log scale to highlight behavior in the boundary layer.
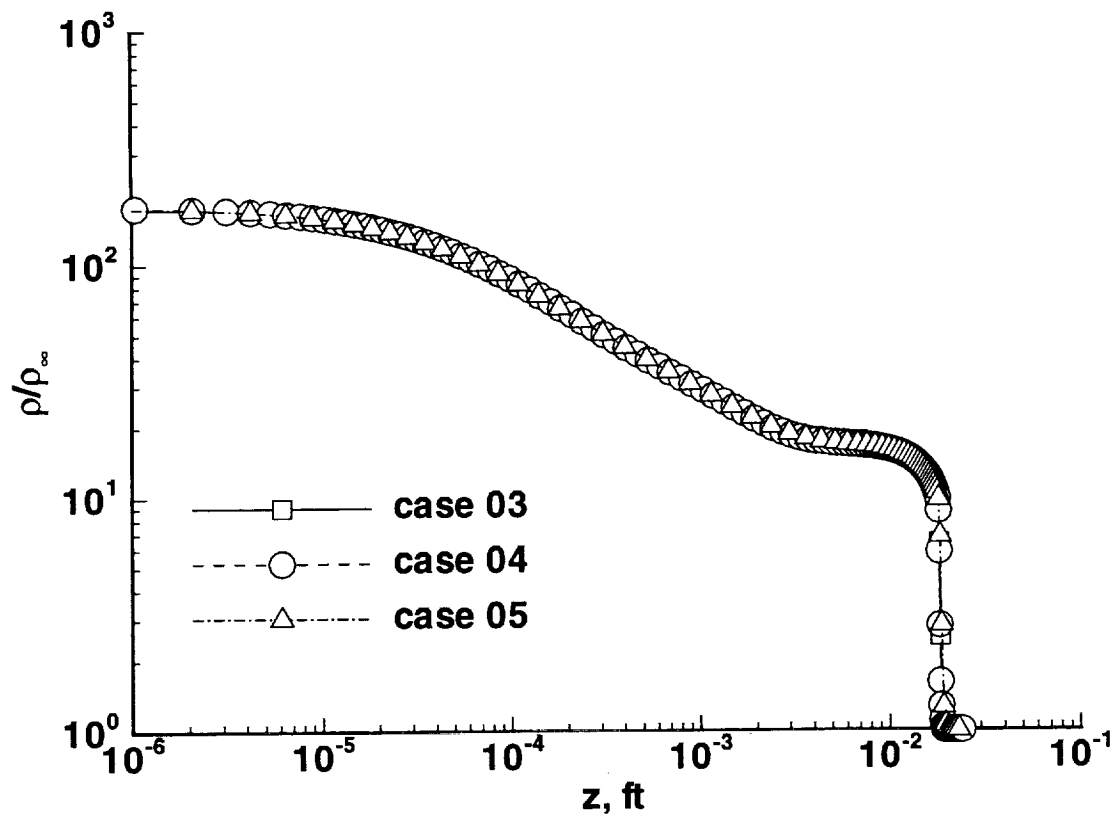
Figure 16: Density profile across shock layer adjacent to the stagnation streamline for cases 03, 04 and 05 involving a 7 species air model using a log scale to highlight behavior in the boundary layer.
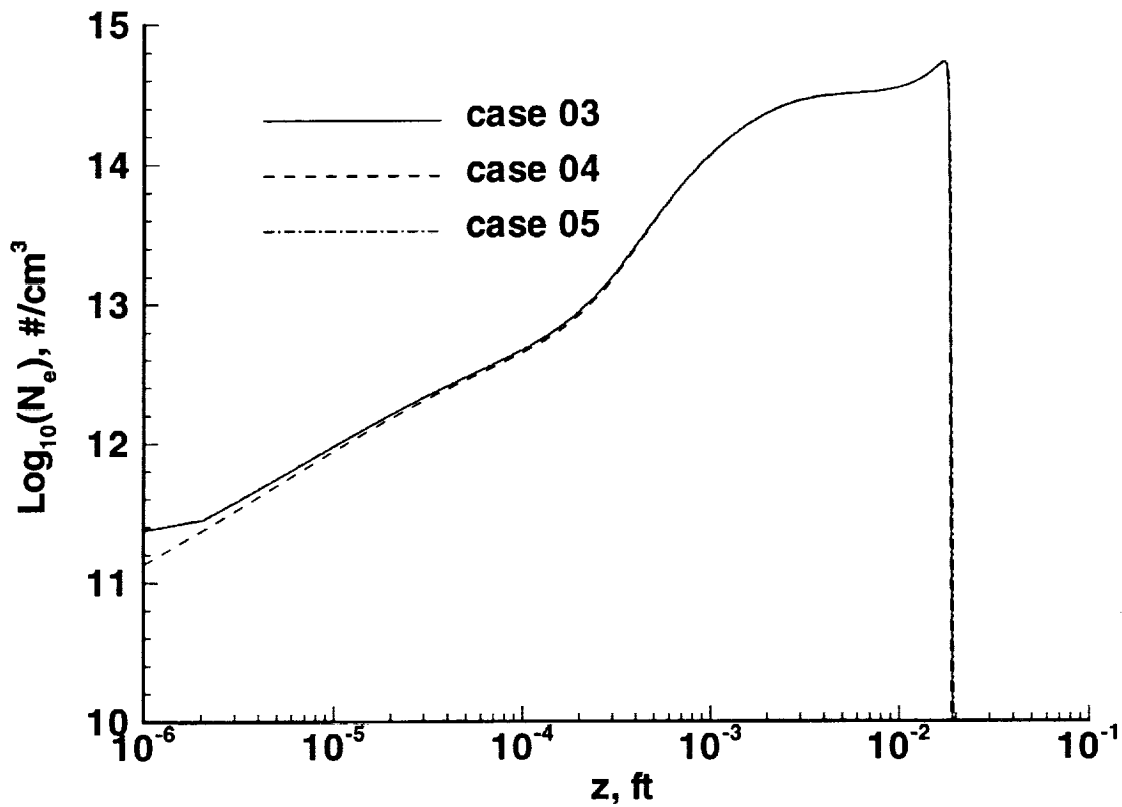
Figure 17: Electron number density profile across shock layer adjacent to the stagnation streamline for cases 03, 04 and 05 involving a 7 species air model using a log scale to highlight behavior in the boundary layer.
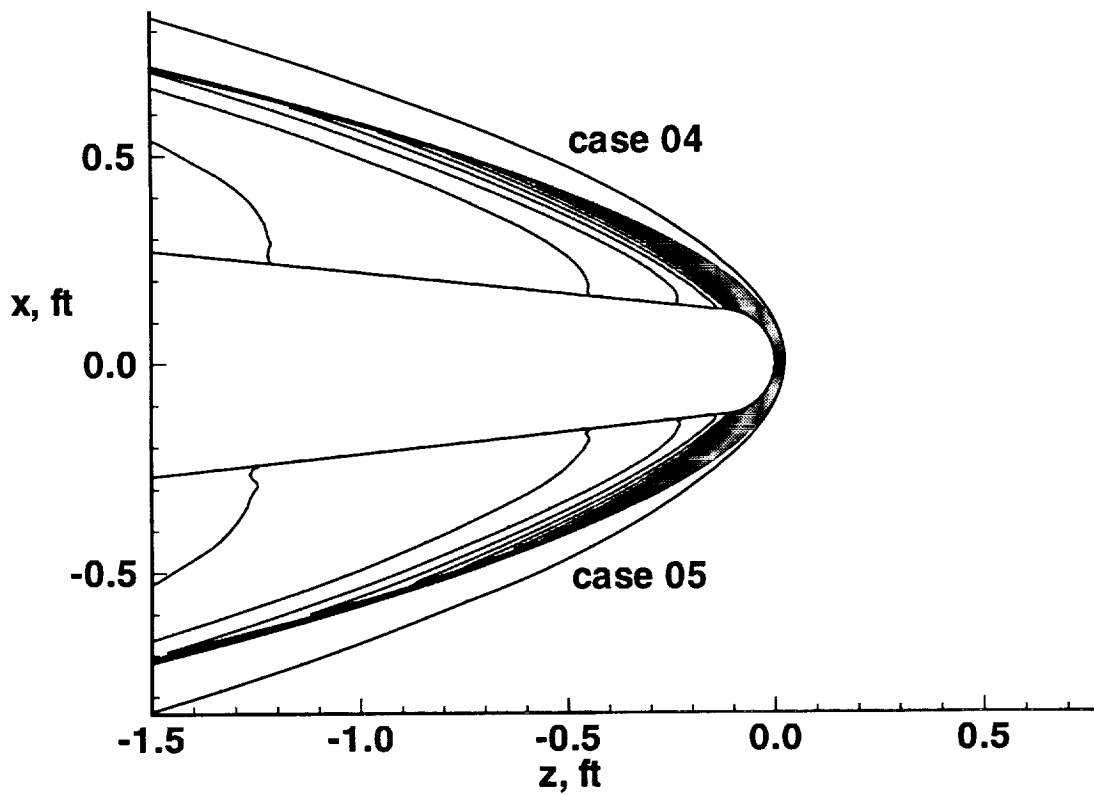
Figure 18: Pressure contours over the forward part of the wedge with $\Delta p/\rho_\infty V_\infty^2 = .01$. The upper symmetry plane is from case 04 and the lower symmetry plane is from case 05.
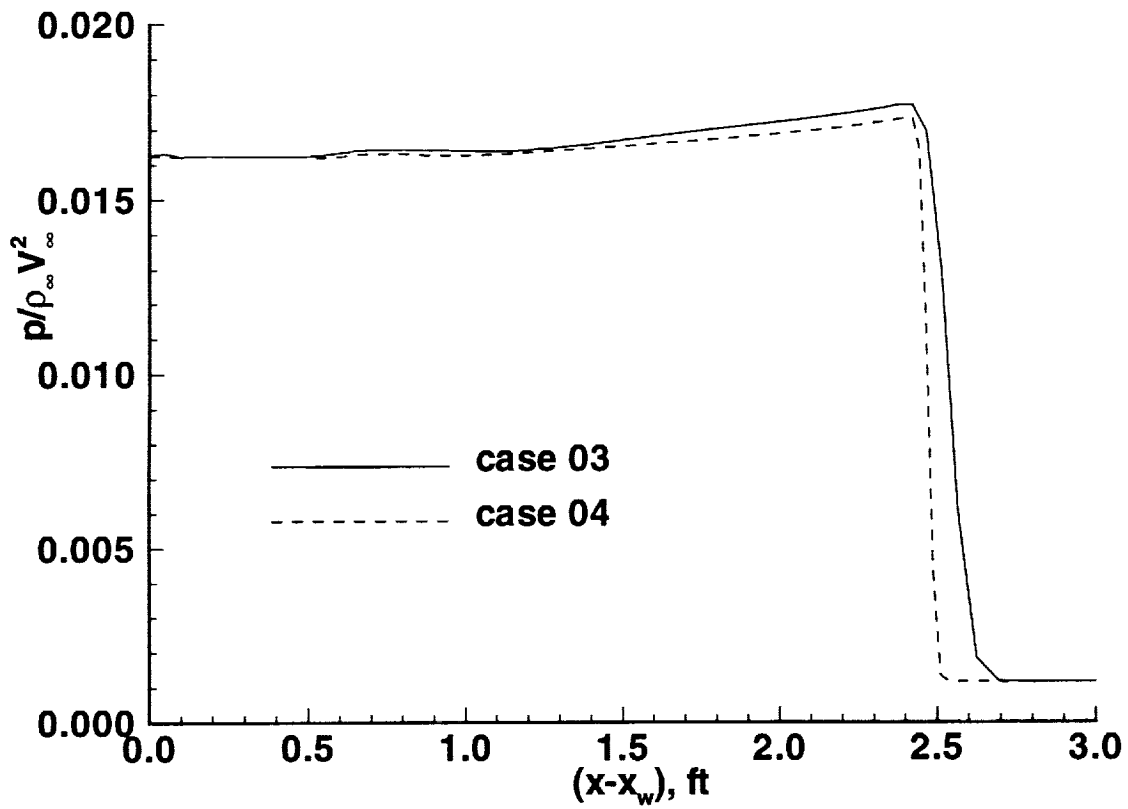
Figure 19: Pressure profile across shock layer at the exit plane for cases 03 and 04 involving a 7 species air model.
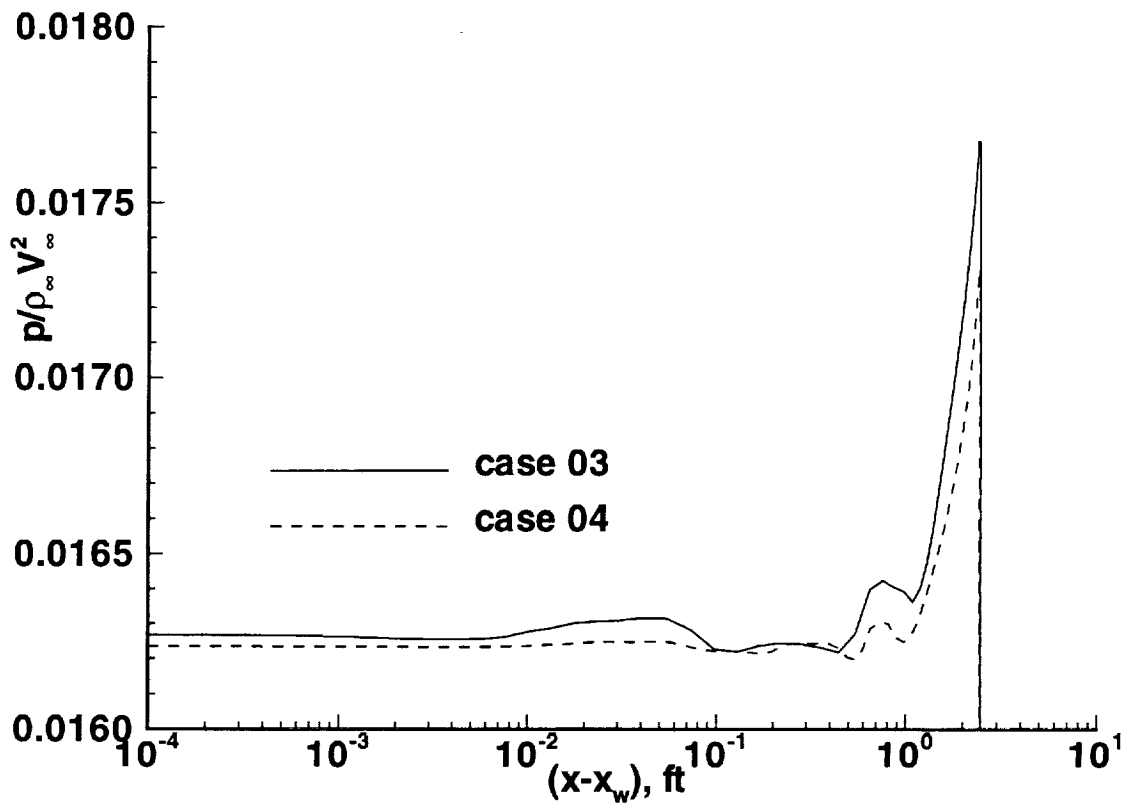
Figure 20: Pressure profile across shock layer at the exit plane for cases 03 and 04 involving a 7 species air model using a log scale to highlight behavior in the boundary layer.
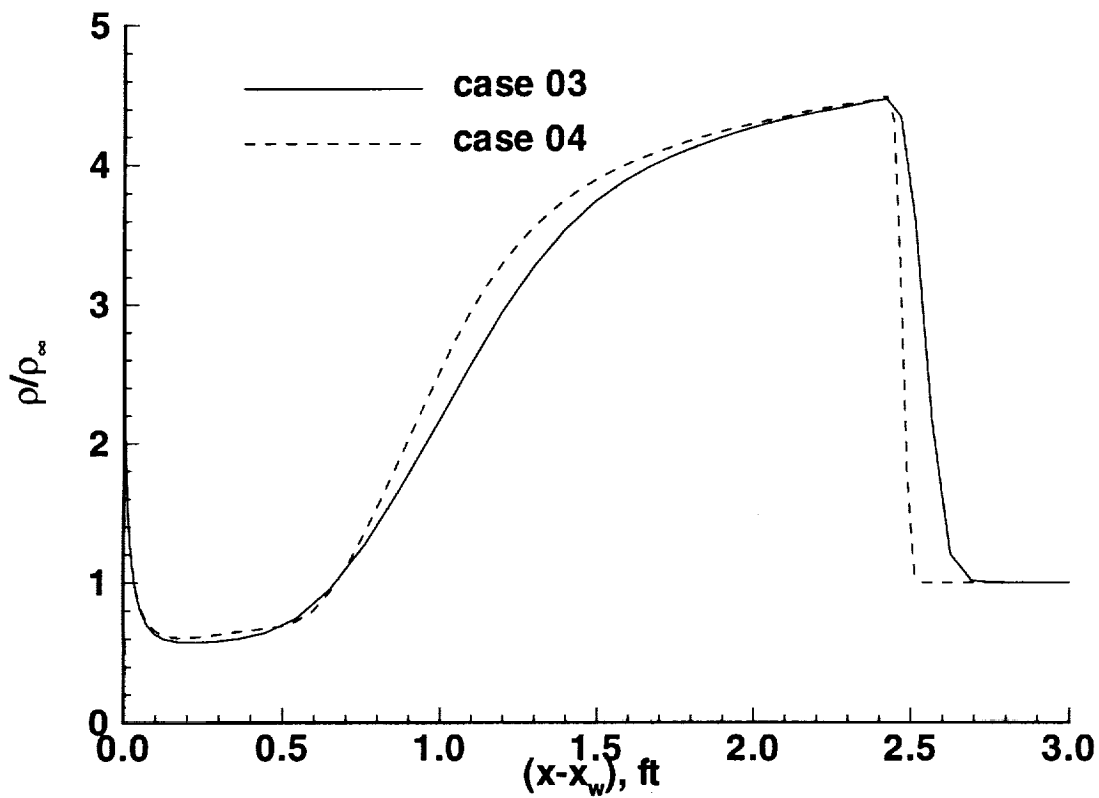
Figure 21: Density profile across shock layer at the exit plane for cases 03 and 04 involving a 7 species air model.
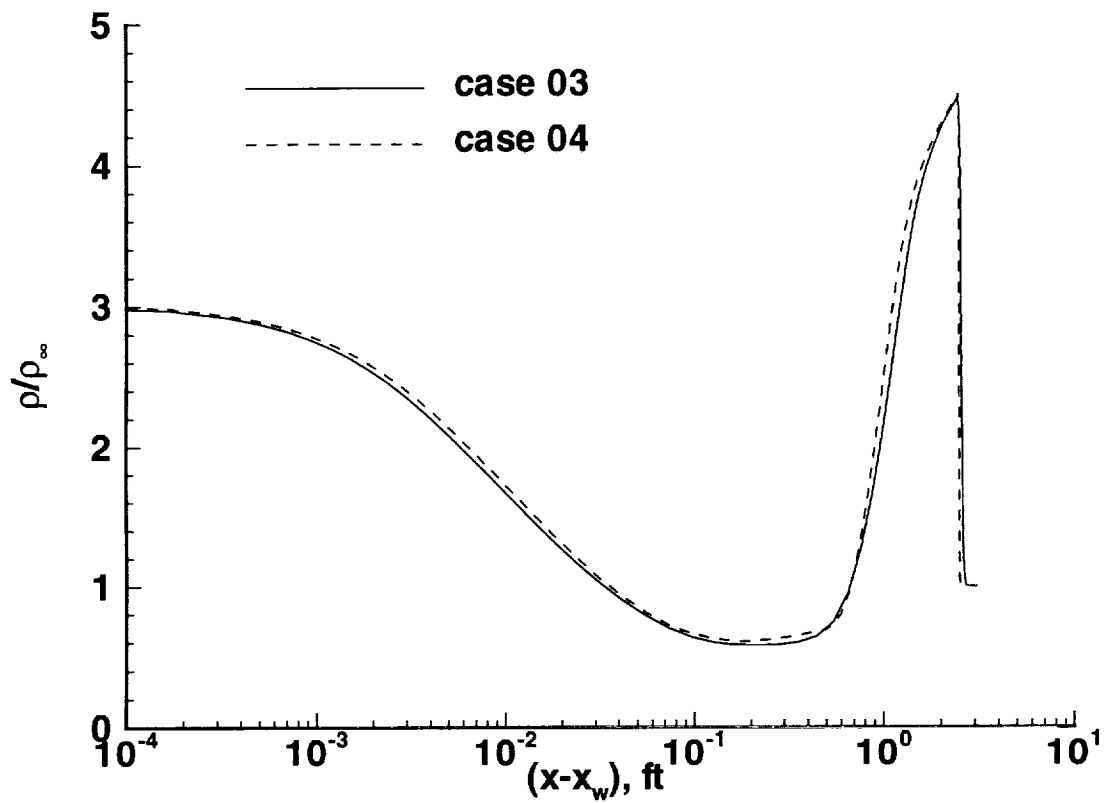
Figure 22: Density profile across shock layer at the exit plane for cases 03 and 04 involving a 7 species air model using a log scale to highlight behavior in the boundary layer.
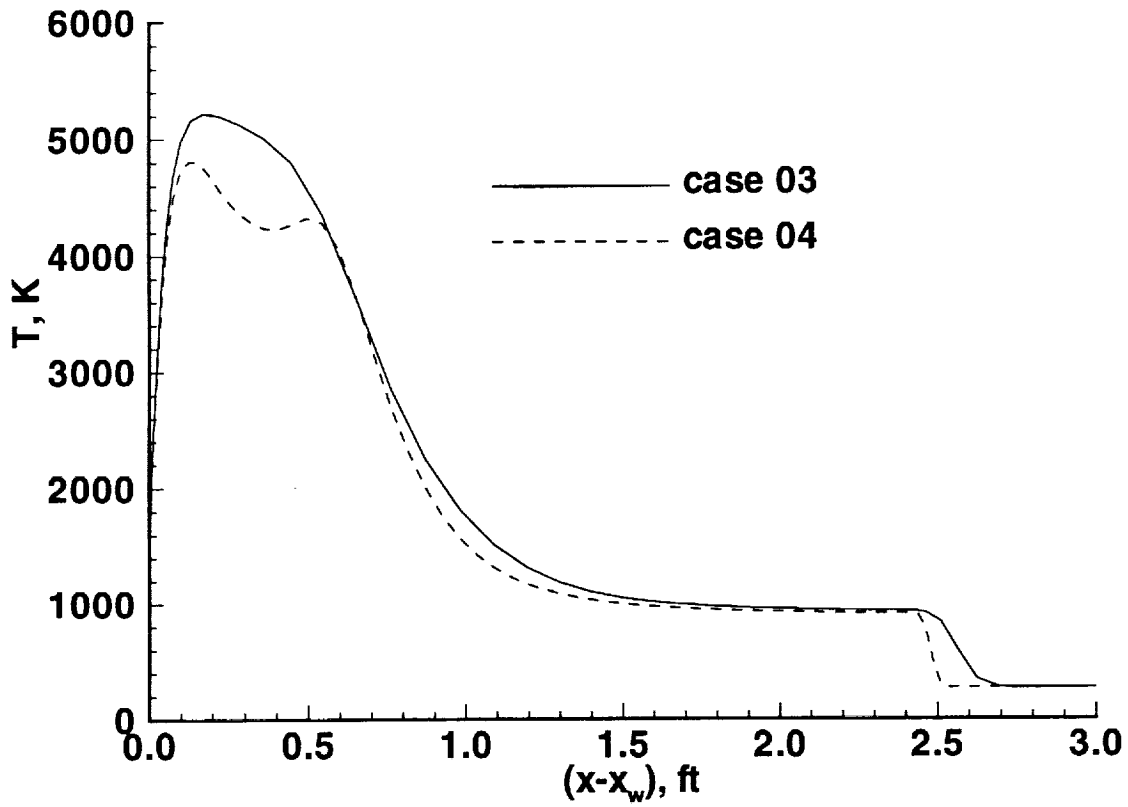
Figure 23: Temperature profile across shock layer at the exit plane for cases 03 and 04 involving a 7 species air model.
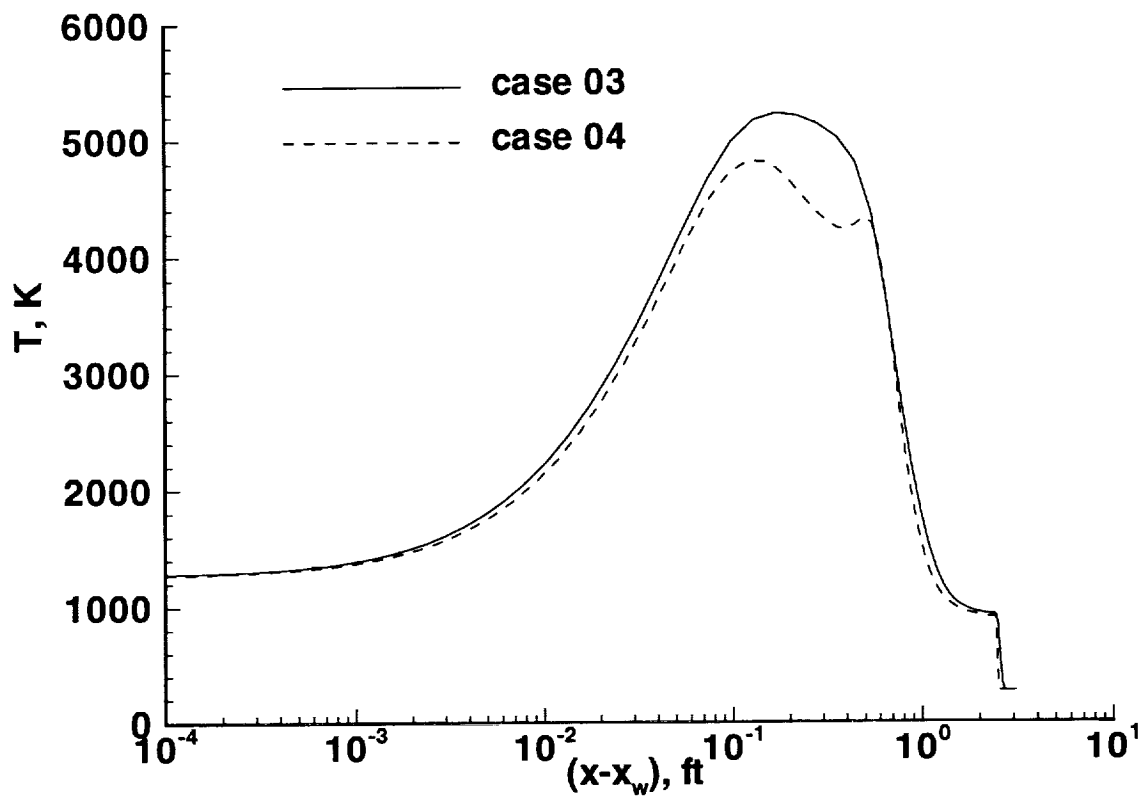
Figure 24: Temperature profile across shock layer at the exit plane for cases 03 and 04 involving a 7 species air model using a log scale to highlight behavior in the boundary layer.
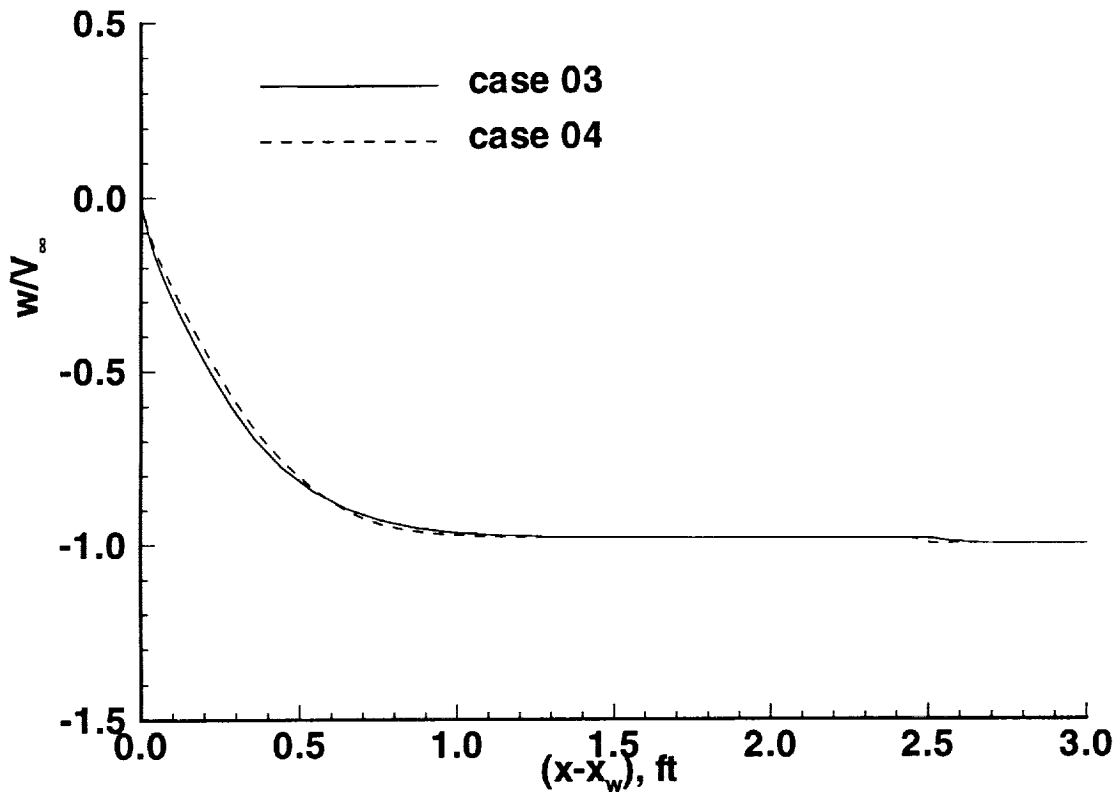
Figure 25: The w velocity component profile across shock layer at the exit plane for cases 03 and 04 involving a 7 species air model.
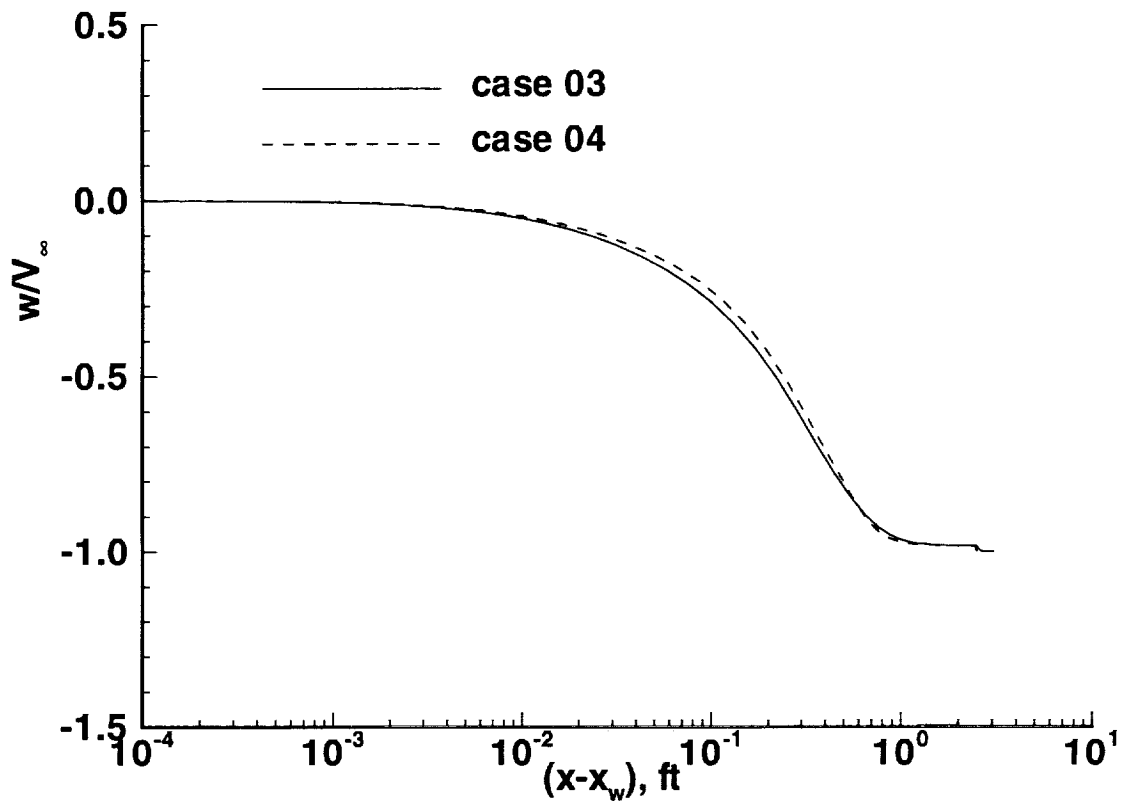
Figure 26: The w velocity component profile across shock layer at the exit plane for cases 03 and 04 involving a 7 species air model using a log scale to highlight behavior in the boundary layer.
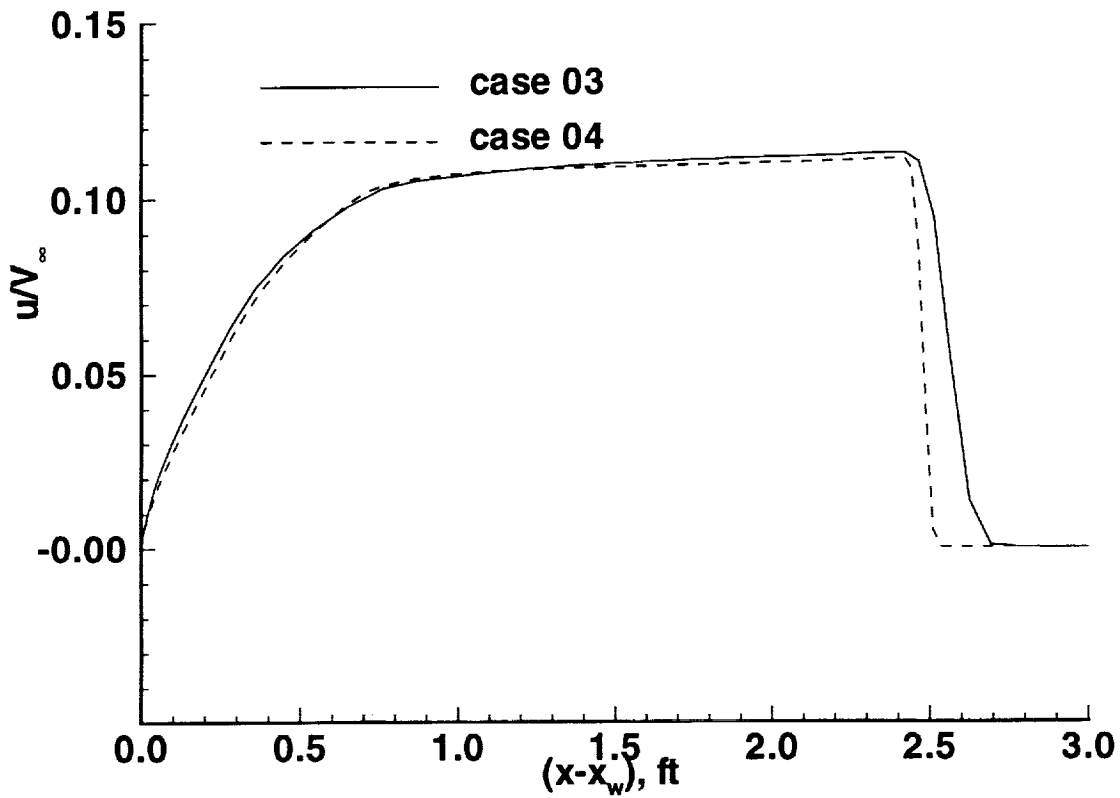
Figure 27: The u velocity component profile across shock layer at the exit plane for cases 03 and 04 involving a 7 species air model.
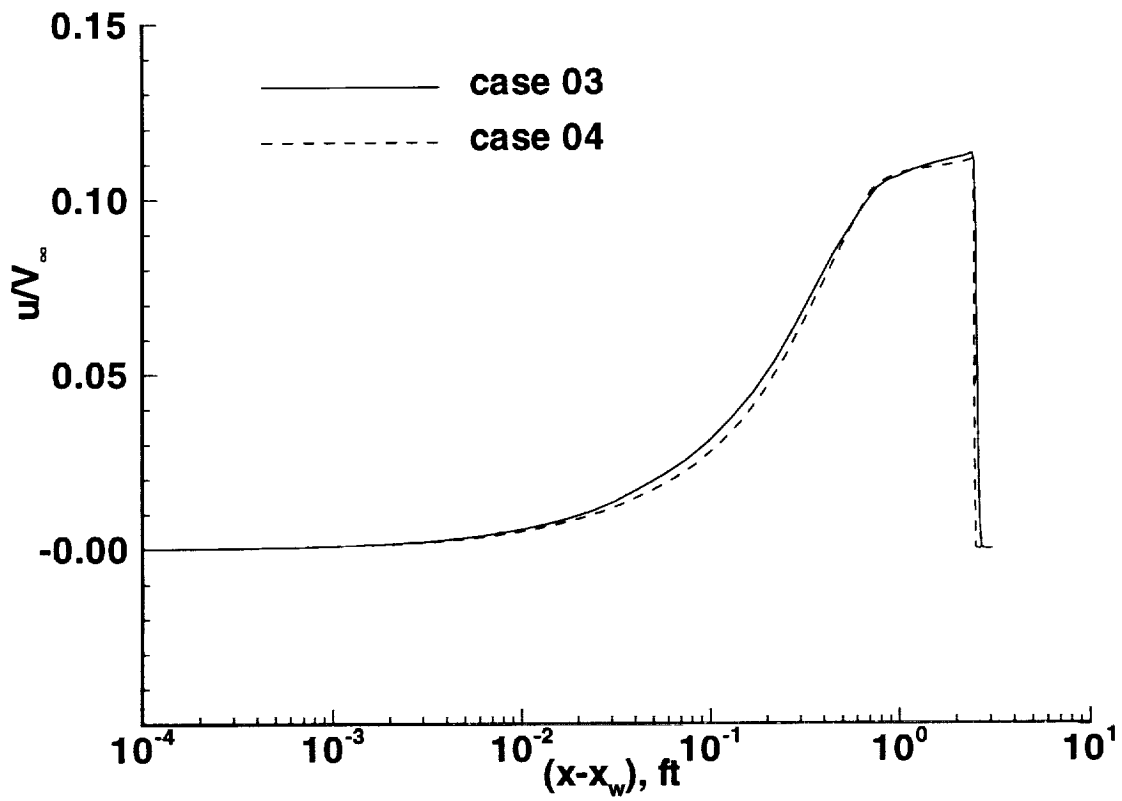
Figure 28: The u velocity component profile across shock layer at the exit plane for cases 03 and 04 involving a 7 species air model using a log scale to highlight behavior in the boundary layer.
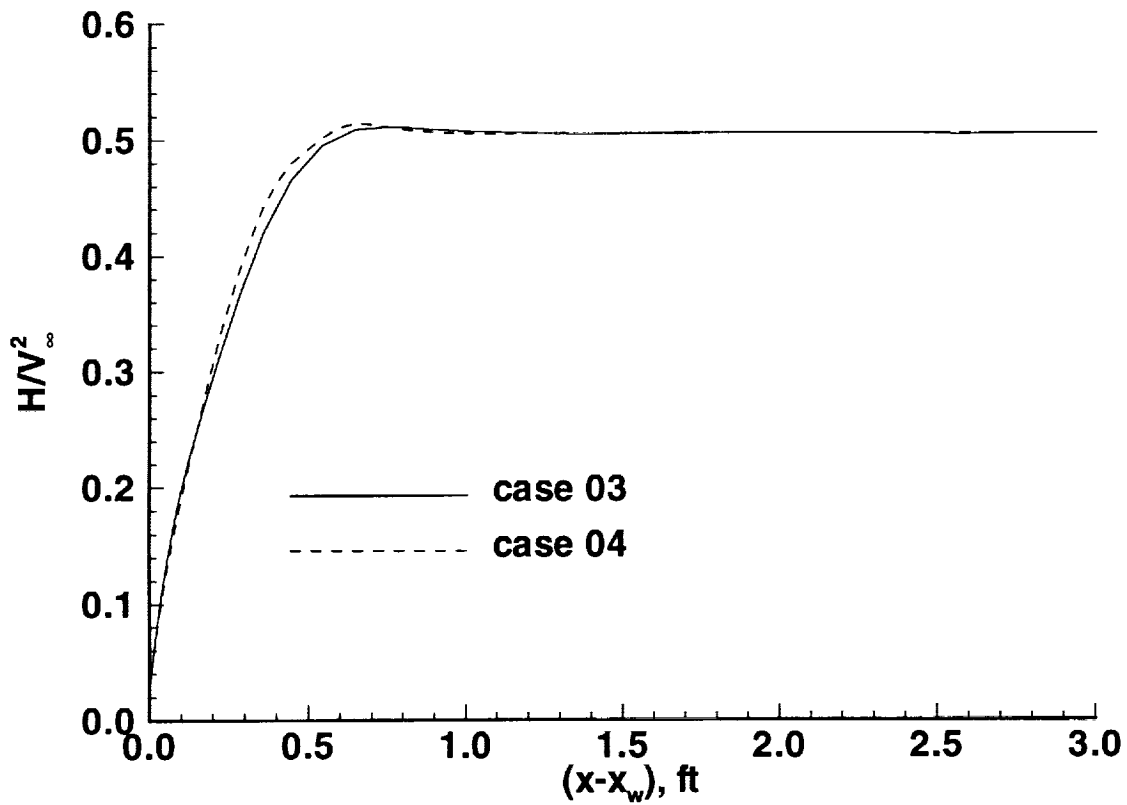
Figure 29: Total enthalpy profile across shock layer at the exit plane for cases 03 and 04 involving a 7 species air model.
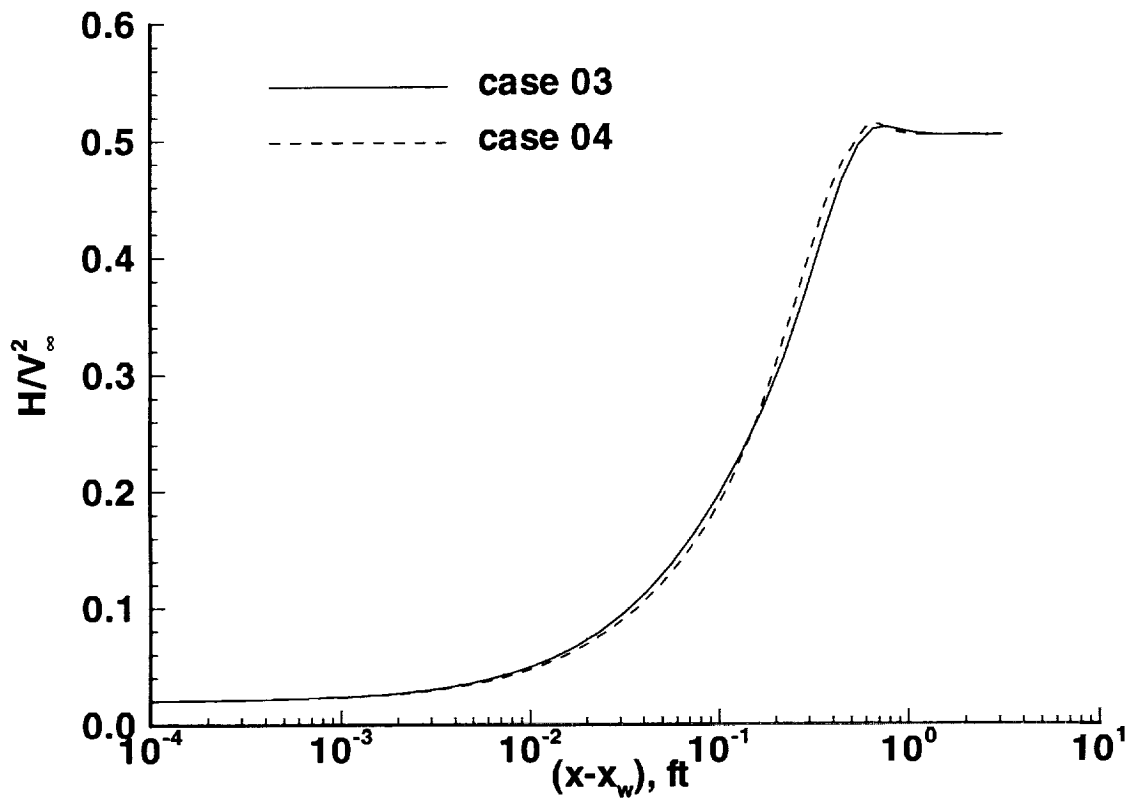
Figure 30: Total enthalpy profile across shock layer at the exit plane for cases 03 and 04 involving a 7 species air model using a log scale to highlight behavior in the boundary layer.
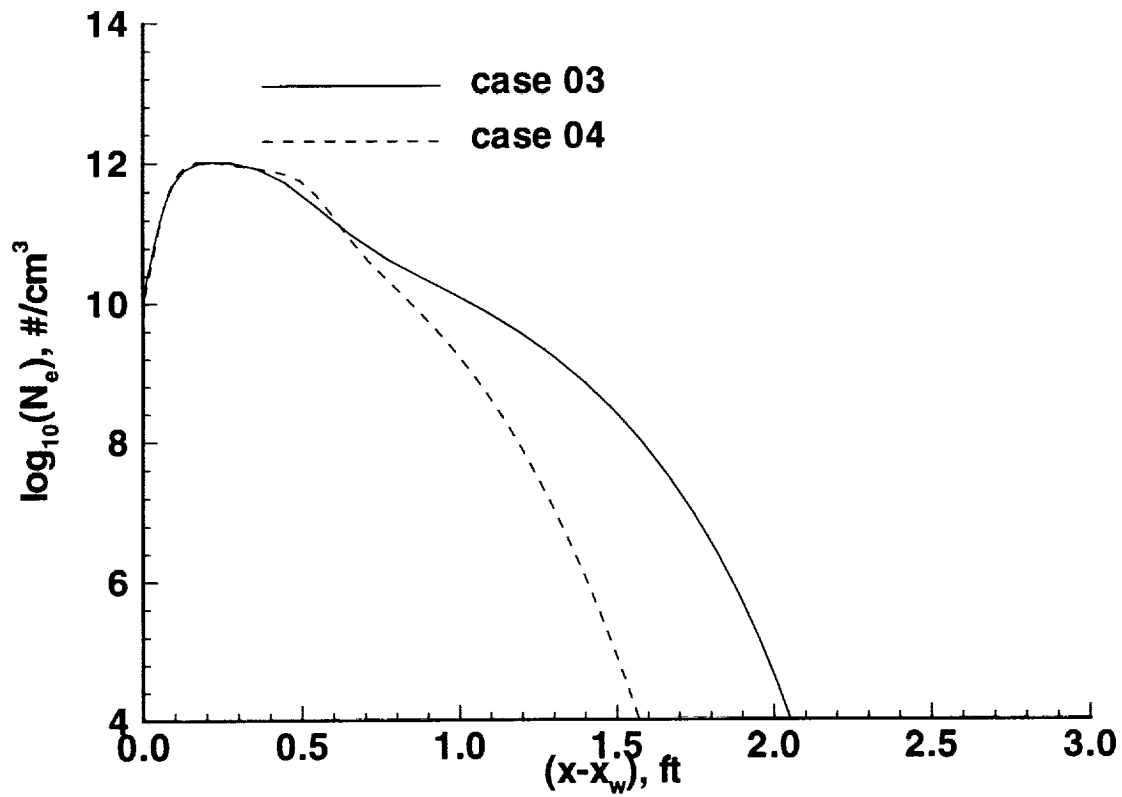
Figure 31: Electron number density profile across shock layer at the exit plane for cases 03 and 04 involving a 7 species air model.
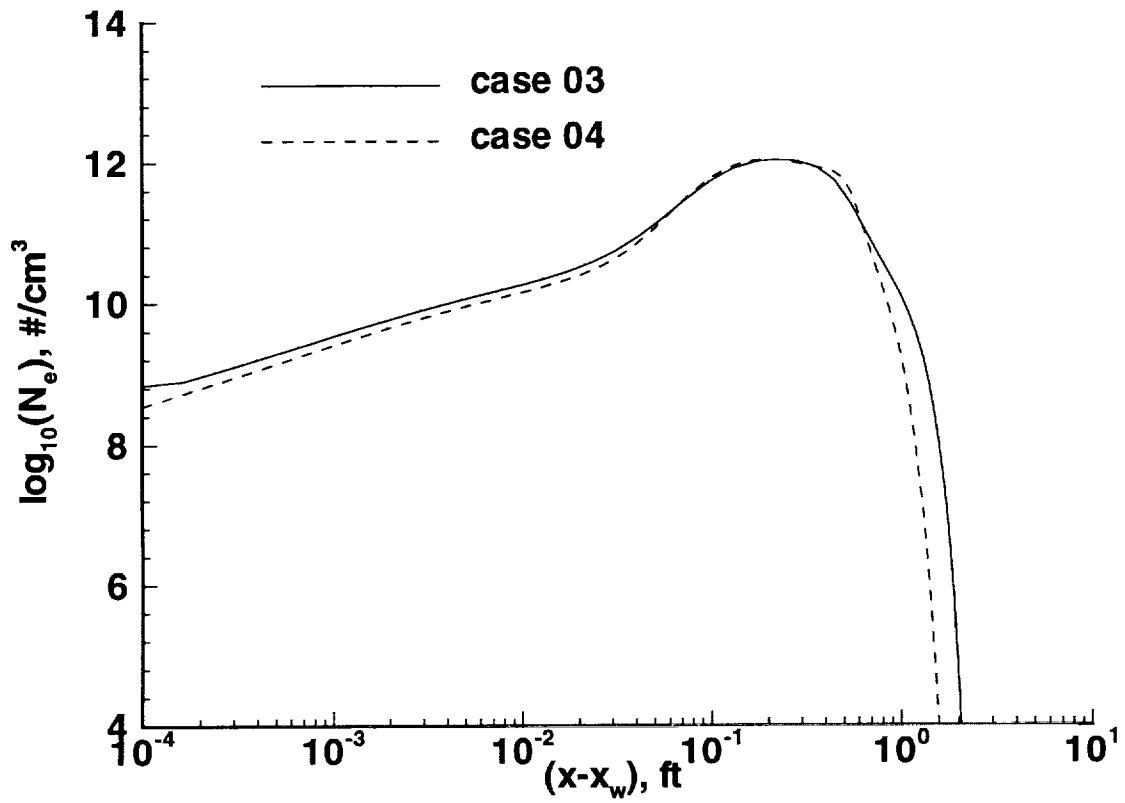
Figure 32: Electron number density profile across shock layer at the exit plane for cases 03 and 04 involving a 7 species air model using a log scale to highlight behavior in the boundary layer.

REPORT DOCUMENTATION PAGE

Public reporting burden for this collection of information is estimated to average 1 hour per response, including the time for reviewing instructions, searching existing data sources, gathering and maintaining the data needed, and completing and reviewing the collection of information. Send comments regarding this burden estimate or any other aspect of this collection of information, including suggestions for reducing this burden, to Washington Headquarters Services, Directorate for Information Operations and Reports, 1215 Jefferson Davis Highway, Suite 1204, Arlington, VA 22202-4302, and to the Office of Management and Budget, Paperwork Reduction Project (0704-0188), Washington, DC 20503.

1. AGENCY USE ONLY (Leave blank)	2. REPORT DATE August 1993	3. REPORT TYPE AND DATES COVERED Technical Memorandum

4. TITLE AND SUBTITLE

Hypersonic, Nonequilibrium Flow Over a Cylindrically Blunted 6° Wedge

5. FUNDING NUMBERS

506-40-91-02

6. AUTHOR(S)

Peter A. Gnoffo

7. PERFORMING ORGANIZATION NAME(S) AND ADDRESS(ES)

NASA Langley Research Center
Hampton, VA 23681-0001

8. PERFORMING ORGANIZATION REPORT NUMBER

9. SPONSORING/MONITORING AGENCY NAME(S) AND ADDRESS(ES)

National Aeronautics and Space Administration
Washington, DC 20546-0001

10. SPONSORING/MONITORING AGENCY REPORT NUMBER

NASA TM-108994

11. SUPPLEMENTARY NOTES

Peter A. Gnoffo: Langley Research Center, Hampton, VA.

12a. DISTRIBUTION/AVAILABILITY STATEMENT

Unclassified-Unlimited

Subject Category 34

12b. DISTRIBUTION CODE

13. ABSTRACT (Maximum 200 words)

The numerical simulation of hypersonic flow in chemical nonequilibrium over a cylindrically blunted 6° wedge is described. The simulation was executed on a Cray C-90 with Program LAURA 92-v1. Code setup procedures and sample results, including grid refinement studies and variations of species number are discussed. This simulation relates to a study of wing leading edge heating on transatmospheric vehicles.

14. SUBJECT TERMS

Langley Aerothermodynamic Upwind Relaxation Algorithm (LAURA)

15. NUMBER OF PAGES

38

16. PRICE CODE

A03

17. SECURITY CLASSIFICATION OF REPORT Unclassified	18. SECURITY CLASSIFICATION OF THIS PAGE Unclassified	19. SECURITY CLASSIFICATION OF ABSTRACT	20. LIMITATION OF ABSTRACT